Directional Conversion of a THz Propagating Wave into Surface Waves in Deformable Metagratings

JIAMING LIU,[1] XU FANG,[2,3] FEI HE,[2] SHENGQI YIN,[2] WEN LYU,[1] HUA GENG,[1] XIAOJIAO DENG,[1] AND XIAOPING ZHENG[1,4]

[1] *Department of Automation, Tsinghua University, Beijing 100084, China*
[2] *School of Electronics and Computer Science, University of Southampton, SO17 1BJ, UK*
[3] *x.fang@soton.ac.uk*
[4] *asean@mail.tsinghua.edu.cn*

Abstract: Controllable conversion between propagating light waves and surface waves (SWs) has recently attracted significant research interests. This paper demonstrates, via numerical simulation, for the first time all-dielectric SW converters that possess a tunable and directional SW conversion efficiency. The SW converters contain multiple metagratings of Si pillars embedded in a deformable substrate. In the analysis, an infinitely large, bi-periodic metagrating under the illumination of linearly polarized light is considered first. The SW conversion efficiency of this metagrating can be modulated between 4.3% and 51.0% for incident light frequency at 0.8 THz, by stretching the deformable substrate along the direction of SW propagation. Subsequently, two SW converters under circularly polarized light illumination are analyzed, where a similar level of efficiency modulation is retained in finite-sized metagratings. In these converters, only the metagrating channels along the stretch direction have a strong SW conversion efficiency, which can reach 40.4% after normalization against the effective grating area. The directivity, a parameter defined here to reveal the energy contrast among the output channels, reaches 38.6 in one of the converters. Due to its high tunability, high directivity and compact size, the SW converters may be used as tunable optical sensors and light couplers in the THz regime.

1. Introduction

Electromagnetic surface wave (SW) converters are devices that transfer freely propagating waves (PW) into SWs. Traditional SW converters, such as metal grating couplers and glass prisms, often lack tunability and/or are too large for integrated applications. Several different kinds of metasurfaces, planar arrays of electromagnetic resonators, are recently proposed as compact, multifunctional SW converters [1-6]. These two-dimensional artificial structures can induce a rapid and controllable phase variation within a subwavelength thickness, allowing for unprecedented control over light wavefronts [7-9]. Many light manipulation applications have been explored based on metasurfaces, including anomalous reflection/refraction [10-12], beam focusing [13-15], optical holograms (i.e. meta-holograms) [16,17], polarimeters [18], as well as SW converters [1-6], the topic of this work.

From the perspective of constituent materials, metasurface research started with plasmonic materials, following by the more recent exploration of dielectrics (i.e. the all-dielectric metasurfaces) [19-22]. The huge research interests in all-dielectric metasurfaces originate from their low light absorption. For high-efficiency wave manipulation, this is tremendously beneficial, especially at frequencies above the GHz range. In addition, dielectric resonators possess localized multipole resonances, which allow for a high level of wavefront manipulation using relatively simple nano- and microstructures [23]. A wide range of devices (e.g. metalenses and meta-holograms) has been demonstrated by using all-dielectric metasurfaces [13,14,16].

Nevertheless, to the best of our knowledge, there has been no report on PW-SW conversion using all-dielectric meta-couplers that allow for low-loss, ~90° light bending. In the first part of this work, we propose and numerically analyze all-dielectric metagratings that function as high-efficiency, tunable SW couplers in the THz (terahertz) region. By using these metagratings as elementary channels, we further demonstrate two types of multichannel SW converters that facilitate tunable and directional SW conversion.

2. Device schematic

Figure 1 schematically illustrates one of the multichannel SW converters. The converter has three SW channels that are based on three identical, finite-sized metagratings. Metagratings, as opposed to phase-gradient metasurfaces, are used here for their capability to achieve a large angle change in the wave propagating direction (here a change of approximately 90° is required, in order to convert a normal incident wave to a plane wave) [24]. Each metagrating is an array of Si pillars embedded in a deformable PDMS (polydimethylsiloxane) substrate. As discussed in details below, the intended functionality of the converter is to create a contrast in the conversion efficiency among the channels, via controlled deformation of the substrate.

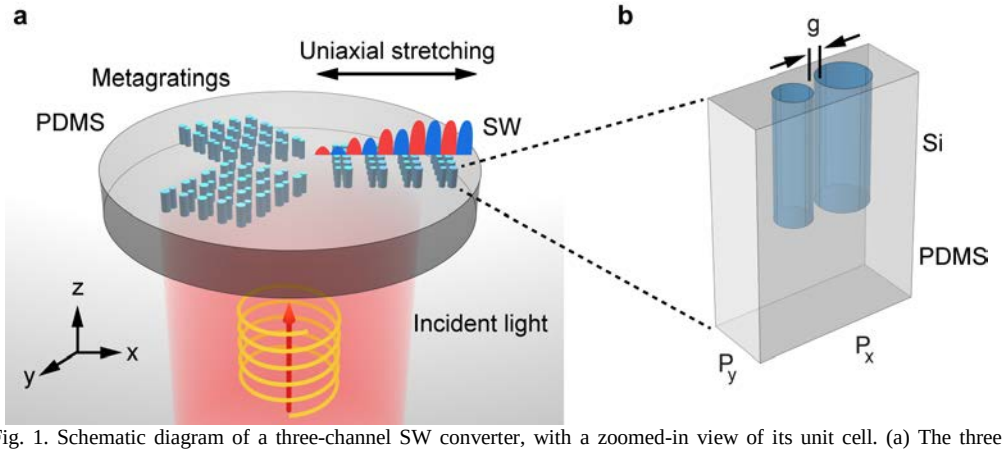

Fig. 1. Schematic diagram of a three-channel SW converter, with a zoomed-in view of its unit cell. (a) The three metagrating channels are distributed uniformly in the azimuthal direction in the converter. Each metagrating is an array of Si pillars embedded in a PDMS substrate. The converter is illuminated at normal incidence (i.e. along the +z direction) by circularly polarized light from the PDMS side. Without any substrate deformation, the three output channels have an identical and low SW conversion efficiency. Stretching the PDMS substrate along the axis of a specific channel (here the x axis) can enhance the conversion efficiency of this channel by an order of magnitude, creating directional SW conversion. (b) The unit cell contains two closely spaced Si pillars. The two pillars have the same height of 265 μm, and their diameters are 76 μm and 108 μm. The gap between the two pillars (g) and the periodicity along the x and y axis (P_x and P_y, respectively) change with the magnitude of substrate deformation.

As a proof-of-principle demonstration, the two converters discussed in this work (i.e. the three-channel converter shown in Fig. 1 and a four-channel converter discussed in Section 6) are both designed to work at light frequency of 0.8 THz, which corresponds to a free-space wavelength λ_0 of 375 μm. The incident light illuminates the metagratings at normal incidence from the PDMS side [Fig. 1(a)].

As discussed in details in Sections 3-5, the geometric parameters of the metagrating are judiciously chosen, by using both analytical equations and numerical simulation. The height of the two pillars in a unit cell is 265 μm, and their diameters are 76 μm and 108 μm. These values stay unchanged during substrate deformation. The other three parameters, the unit cell size along the axis of mirror symmetry [i.e. P_x in Fig. 1(b)], the size in the orthogonal planar direction [i.e. P_y in Fig. 1(b)], and the inter-pillar gap size g, all change with substrate strain. Without any strain, P_x, g, and P_y are 290 μm, 19 μm, and 174 μm, respectively. Figure 1(a)

illustrates excitation of SW in only one of the three output channels in a stretched converter, and the corresponding values of P_x, g, and P_y of this favored channel (i.e. the channel along the *x* axis, termed as the 0° channel in Section 6) are 370 μm, 24 μm, and 150 μm, respectively.

The numerical simulation is conducted by using a commercial finite element solver (COMSOL Multiphysics). Both non-periodic, isolated scattering units and periodic arrays are simulated, using boundary settings discussed in our recent works [15,25]. Si is treated as a lossless material with a dielectric constant of 11.67 [26]. PDMS is slightly absorptive, and its dielectric constant and loss tangent are 2.35 and 0.03, respectively [27]. Due to the lack of reliable THz measurement data on their strain dependence, these two values are assumed independent of the substrate deformation.

3. Initial parametric search based on two design principles

In this section, we discuss two principles for designing the SW conversion metagrating, which follow those derived for metalenses with high numerical apertures [24,28]. These principles, assisted with preliminary numerical simulation, are used to identify initial geometric parameters for realizing high-efficiency SW conversion. The results form the basis of the discussion on device characterization and optimization in Sections 4 and 5.

The first principle states that, at normal incidence (i.e. the illumination configuration here), the grating should produce a very limited number of propagating diffraction orders, as well as at least one non-propagating diffraction order that is almost parallel to the surface. The propagating orders have to be limited in the number, as they can compete with the non-propagating orders in sharing the incident energy. Meanwhile, the non-propagating orders need to match the SW in the in-plane wave momentum. This principle restricts the periodicity of the metagrating. Here, as the incident light comes from the PDMS side (Fig. 1), the transmitted and the reflected light propagates in the air and the PDMS substrate, respectively. Light transmission consequently follows the grating formula of

$$m\,\lambda_0 = p\,(n_t\,sin\theta_t - n_i\,sin\theta_i) \tag{1}$$

where m is the diffraction order, and p is the grating periodicity along the diffraction direction. θ_i and θ_t are the angle of incidence and refraction, respectively, and n_i and n_t are the refractive indices of the two media (i.e. PDMS and air). For light reflection, the grating formula becomes

$$n\,\lambda_0 = p\,n_i\,(sin\theta_r - sin\theta_i) \tag{2}$$

where θ_r is the angle of reflection order *n*.

Following this design principle, P_x (i.e. the grating periodicity along the *x* axis) can be set as 370 μm, slightly smaller than λ_0. Based on Eqs. (1) and (2), this value ensures that only R_0, R_{-1}, R_{+1} and T_0 (i.e. the 0, -1 and +1 orders of reflection and the zeroth-order transmission) exist as propagating orders in the *xz* plane. Meanwhile, the non-propagating $T_{\pm1}$ orders (i.e. the -1 and the +1 orders of transmission) are about to emerge from the air-PDMS interface. As we are only interested in unidirectional SW propagation along the *x* axis in this work, P_y (i.e. the grating periodicity along the *y* axis) is set as 150 μm, a value small enough to eliminate any high-order diffraction in the *yz* plane.

The second design principle states that, for an individual light scattering unit, it needs to produce strong light scattering along the air-PDMS interface. This principle can be satisfied by judiciously designing the light scattering unit, here the two Si pillars in Fig. 1(b). There are four geometric parameters to determine, the diameters of the two pillars, their height (set as identical for the two pillars), and the inter-pillar gap size g. The pillar diameters are chosen as 76 μm and 108 μm based on experience accumulated in recent research projects. As a crucial value that is actively modulated via substrate deformation, the gap g is temporally set here as 24 μm, to allow for determining the pillar height.

The pillar height is determined numerically, a process that is assisted by analyzing the resonance modes [29]. Three major resonance modes exist in a pair of Si pillars, determined by analyzing the cross sections and assuming an infinite pillar height (see the Supplementary Information for details). All the three modes radiate into the air, with the two pillars viewed as truncated, open resonators [30], and the total output field is the vector sum of these three modes. After a few rounds of optimization based on analyzing light scattering pattern, we find that 265 μm is a suitable value for the pillar height. This value is consequently chosen, and it remains unchanged throughout this work.

4. Influence of two critical geometric parameters

As discussed in Section 3, we use the first and second design principles to identify suitable grating periodicity and unit cell geometry, respectively, and arrive at an initial metagrating design. In this section, we numerically test the SW conversion performance of the design, and further explore its dependence on two crucial geometric parameters, P_x and g.

Both P_x and g are crucial parameters in this work, because of these two reasons: (1) they can significantly influence the SW conversion efficiency, based on the analysis and preliminary numerical simulation discussed in Section 3; (2) they change with substrate deformation. By comparison, although the pillar height and diameters also play an important role in shaping the light scattering pattern, they stay invariant with substrate deformation and consequently do not actively contribute to dynamic SW tuning. Meanwhile, although P_y also changes with substrate deformation, it has little influence on the SW that propagates along the *x* axis.

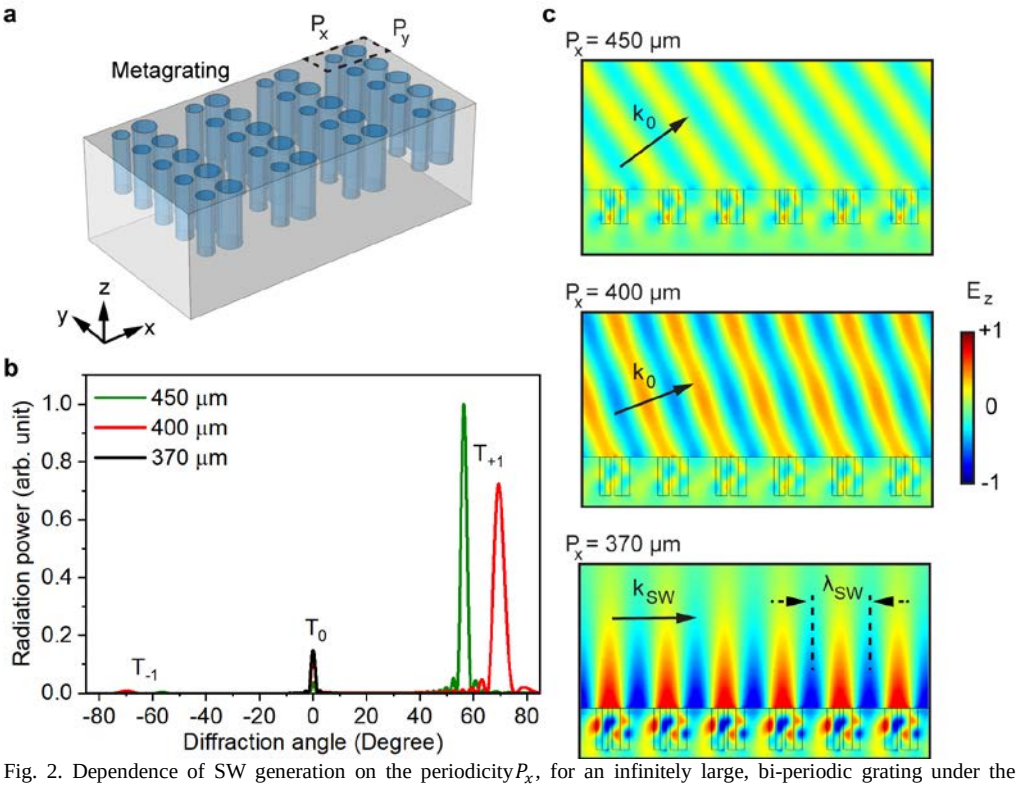

Fig. 2. Dependence of SW generation on the periodicity P_x, for an infinitely large, bi-periodic grating under the illumination of *x*-polarized incident light. (a) Schematic of a section of the Si metagrating. The in-plane direction from the small pillar to the large pillar is along the *+x* direction. (b) Far-field radiation power for three different metagratings. P_x varies as 370 μm, 400 μm and 450 μm, while g and P_y stay as 24 μm and 150 μm, respectively. All the three curves are normalized against the peak value of T_{+1} at $P_x = 450\ \mu m$. The curve of $P_x = 370\ \mu m$ has only one peak of T_0, and

it almost overlaps with the T_0 peaks at $P_x = 400\ \mu m$. None of the curve has a clearly discernable T_{-1} peak. (c) Corresponding near-field E_z distribution in the *xz* plane across the centers of a line of pillars. The field amplitude of the three maps is normalized against the same value. The SW wavelength (λ_{SW}) follows the grating periodicity, which is 370 μm. The arrows indicate the wave propagation directions.

We first explore the influence of P_x on the SW conversion efficiency. At this step, g and P_y stay unchanged as 24 μm and 150 μm, respectively, both values mentioned in Section 3. The metagrating is illuminated by an *x*-polarized plane wave that propagates along the +*z* direction. Light scattered by the metagrating into the far field, together with the near-field distribution of the electric field component around the pillars, is numerically simulated and shown in Fig. 2.

When P_x is 400 μm and 450 μm, Eq. (1) indicates that the metagrating produces three diffraction orders, T_{-1}, T_0, T_{+1}, in the transmission. A significant amount of incident energy is expected to be scattered into free space via these diffraction orders, and the SW is expected to be weak or non-existent. Meanwhile, when P_x is 370 μm, Eq. (1) shows that the diffraction orders of T_{-1} and T_{+1} are almost parallel to the air-PDMS interface. SW generation is expected to be favored in this condition.

This analytical prediction is verified in the numerical simulation shown in Fig. 2(b), which captures all the propagating diffraction orders in the air side. When P_x is 450 μm and 400 μm, the T_{+1} order is very pronounced, indicating that a significant amount of input energy is radiated into the air. In sharp contrast, when P_x is 370 μm, the T_{+1} order disappears, and only a weak T_0 order is clearly discernable. This change indicates that at $P_x = 370\ \mu m$, a significant amount of energy can be confined as an SW.

To verify the existence of SW, Fig. 2(c) shows corresponding near-field distributions of the E_z component (i.e. the *z* component of the electric field) at the air-PDMS interface. When P_x equals 450 μm or 400 μm, the field map is dominated by a plane wave leaving the interface into the air, which is the T_{+1} order in Fig. 2(b). In contrast, at $P_x = 370\ \mu m$, the field map shows a pronounced wave confined to the air-PDMS interface. The SW wavelength λ_{SW} is equivalent to P_x, and its propagation constant is given by

$$k_{SW} = 2\pi/\lambda_{SW} = 2\pi/P_x \approx 1.01k_0 > k_0 \tag{3}$$

where k_0 is the propagation constant of the freely propagating light in air. As k_{SW} is larger than k_0, the in-plane wave seen at $P_x = 370\ \mu m$ in Fig. 2(c) is clearly an SW, rather than the projection of an output plane wave onto the surface (the projection of k_0 on the *xy* plane can never be larger than k_0 for a real output angle). It is worth noting that, the coefficient 1.01 in Eq. (3) depends on the value of P_x, as λ_{SW} follows P_x.

The SW in Fig. 2(c) shows interesting characteristics in its field distribution, which are distinct from other guided waves (e.g. surface plasmons on a metal surface, and evanescent waves at the surface of a Si waveguide or a tapered glass fiber). In the air side that contains no microstructures, the SW clearly appears as a wave with alternating red (indicating positive E_z) and blue (negative E_z) peaks moving to in the +*x* direction. By contrast, in the PDMS side that exhibits a rapid in-plane refractive index change, the wave is highly distorted and is mainly localized in the high-index Si. By monitoring the electromagnetic power outflow at the edges of the unit cell, we notice that the energy of the SW is predominantly in the air side; in the PDMS side, the power outflow is not only much smaller, it even reverses its direction as *z* changes. Based on this observation, in the following analysis on SW conversion efficiency, we concentrate on the field in the air side. In the air side, the energy density of the SW decays exponentially along the *z* axis at a rate of $Exp[-z/t]$, where the characteristic depth *t* equals 173 μm.

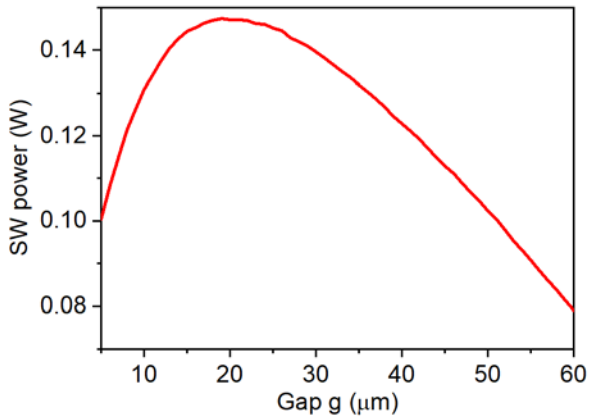

Fig. 3. Influence of gap size g on SW generation, for an infinitely large, bi-periodic grating under the illumination of *x*-polarized incident light. The periodicities P_x and P_y are 370 μm and 150 μm, respectively, and the incident light has a power density of 1 W/mm^2. The SW power reaches a peak value of 0.147 W at $g = 19\ \mu m$.

As discussed in Section 3, the far-field scattering of the unit cell results from the constructive interference of multiple localized resonances. Changing the gap g modifies these resonances, consequently changing the output power into the far field. Figure 3 shows this influence by calculating the power of the generated SW. The values of P_x and P_y stay as 370 μm and 150 μm, respectively, while g is swept from 5 μm to 60 μm. The lower boundary of 5 μm takes into consideration of fabrication feasibility, as nanofabrication processes such as the Bosch process can achieve an aspect ratio of approximately 40 [31]. The SW power is determined as the electromagnetic power passing through an integration widow at the *yz* boundary of the unit cell. Based on the energy distribution of the SW discussed above, the integration window is set to sit on the air-PDMS interface with a height of 500 μm, a value where the SW energy density decays to a negligible value.

With the incident plane wave carrying a power density of 1W/mm^2, the SW power reaches its peak value of 0.147 W with g at 19 μm. The power weakly depends on g within a range of ~10 μm around 19 μm (i.e. approximately between 15 μm and 25 μm). This range covers the initial value of 24 μm, which is used in Section 3 for optimizing the pillar height and in Fig. 2 for the discussion on P_x. Consequently, we choose to continue using $g = 24\ \mu m$ as the target value for high-efficiency SW generation, and conduct the analysis in Sections 5 and 6 using this value.

It is worth noting that, because the metagrating here is infinitely large and nearly lossless, and it is illuminated uniformly by a plane wave that has an infinitely large total incident power, numerical simulation cannot reliably provide a unitless SW conversion efficiency [1]. For this reason, Fig. 3 uses the absolute power of the generated SW to determine the optimal value of g. A unitless conversion efficiency becomes available, once the metagrating or the light beam has a finite size in a planar direction. This condition is satisfied in both Sections 5 and 6 below.

5. Modulating SW generation via substrate deformation

In Section 4, the two most important dimensions P_x and g are tuned independently to explore their respective influence on the SW conversion, in an infinitely large metagrating under the illumination of a uniform plane wave. In this section, we consider a metagrating under uniaxial stretching, where P_x, g and P_y changes simultaneously. We also set a finite width to the incident light, in order to better approximate future experiments and to allow for the extraction of a unitless conversion efficiency.

We start with a metagrating with no substrate strain, where P_x, g and P_y are 290 μm, 19 μm and 174 μm, respectively (Fig. 4). As discussed in details below, these values are chosen to strongly modulate the SW conversion efficiency during substrate deformation. The changes in these three parameters, ΔP_x, Δg and ΔP_y are correlated as

$$\varepsilon = \Delta P_x / P_x = \Delta g / g = -\Delta P_y / (0.5\, P_y) \tag{4}$$

where ε is the uniaxial strain of the PDMS substrate. The coefficient 0.5 is the Poisson's ratio of PDMS, albeit the polymer can have a slightly different Poisson's ratio depending on its composition [32].

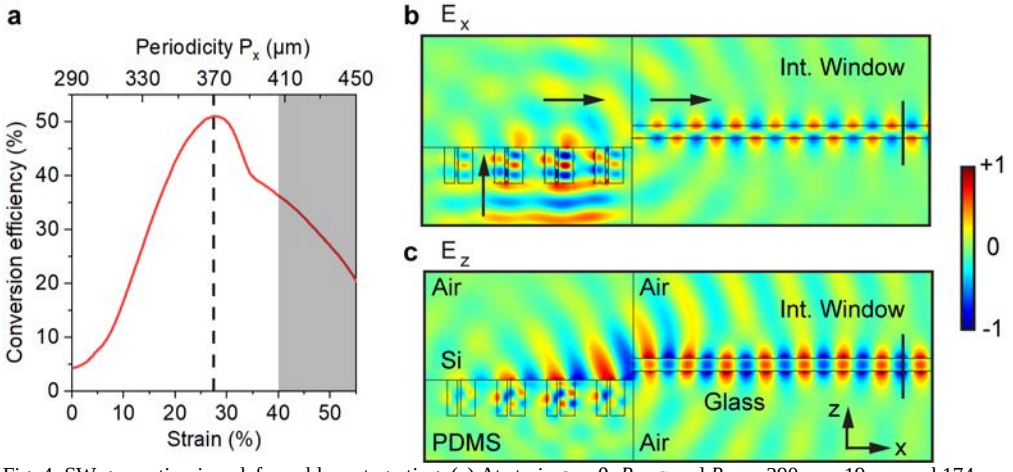

Fig. 4. SW generation in a deformable metagrating. (a) At strain $\varepsilon = 0$, P_x , g and P_y are 290 μm, 19 μm and 174 μm, respectively. At this condition, the conversion efficiency is 4.3%. It reaches the peak value of 51.0% at $\varepsilon = 27.6\%$, which is highlighted by the vertical line. The gray area indicates strain values that are outside the reversible deformation range. (b) E_x component of the electric field around the air-PDMS interface and the glass slab. The strain is at the optimal value of 27.6%. The integration window for computing the SW intensity is 500 μm in height and 2000 μm away from the entrance to the glass slab. The arrows indicate the direction of wave propagation. (c) Corresponding E_z component at the same strain. The incident light, which propagates upwards from the bottom of the maps, is invisible here because the light is *x*-polarized. The field in these two panels is normalized against the same value.

In Fig. 4, the incident light remains *x*-polarized and infinitely wide along the *y* axis, the same as in Section 4. Its width along the *x* axis is now reduced to 1200 μm, covering approximately four unit cells. It is worth noting that, the SW shown in Fig. 2(c) is a type of driven SW [3] rather than an eigenmode of the micro-structured air-PDMS interface, meaning that its stabilized propagation has to be maintained by uniform illumination. (Alternatively, it can be viewed as an eigenmode of the combination of the device and the illumination.) Outside the four unit cells along the *x* axis that are illuminated by the incident light in Fig. 4, the SW quickly scatters into the air and the PDMS substrate.

To estimate the intensity of the driven SW, we use in this work two different methods: by using an integration window at the metagrating boundary to calculate the total power outflow (as seen in Sections 4 and 6), and by using a probe/coupler to channel the driven SW out of the illuminated area (as discussed in this section). In the second method, the probe has to support a self-sustainable eigenmode, as opposed to a driven wave, that provides easy power calculation in simulation and experiment. This approach has been discussed in several recent works, where the probe/coupler appears in a range of different forms [5,6,33]. Here, we choose to use a 93 μm thick glass slab that is placed by the side of the illuminated area [Figs. 4(b) and 4(c)]. Both figures clearly show that most of the SW is coupled into the glass slab as a guided wave. The

SW conversion efficiency of the metagrating is consequently estimated as the energy ratio of the guided wave and the incident light.

Figure 4(a) shows the dependence of the SW conversion efficiency on the substrate strain ε. A broad strain range (0 ~ 55%) is simulated, fully covering the material's reversible deformation range (approximately up to 40% [34]). The conversion efficiency is at a very low level of 4.3% at $\varepsilon = 0$. It gradually increases with ε and reaches its peak value of 51.0% at $\varepsilon = 27.6\%$, representing an efficiency change by an order of magnitude. Further increasing ε beyond 27.6% gradually reduces the efficiency. The planar dimensions at the optimal efficiency are $P_x = 290\ \mu\text{m} \times 127.6\% = 370.04\ \mu\text{m}$, $g = 19\ \mu\text{m} \times 127.6\% = 24.244\ \mu\text{m}$, and $P_y = 174\ \mu\text{m} \times (1 - 0.5 \times 27.6\%) = 149.99\ \mu\text{m}$. These values match with the target values set out in Section 4, which are $P_x = 370\ \mu\text{m}$, $g = 24\ \mu\text{m}$, and $P_y = 150\ \mu\text{m}$.

The curve in Fig. 4(a) can be divided into three distinctive segments, and interpreted by combining the two design principles discussed in Section 3 and the parametric sweeping conducted in Section 4. (1) For ε much smaller than 27.6%, the periodicity P_x is much smaller than the free-space wavelength of 375 μm, and there is no non-propagating diffraction order to provide momentum matching for SW excitation. (2) For ε much larger than 27.5%, most input energy radiates into the free space as the T_{+1} scattering order (e.g. $P_x = 400\ \mu m$ and $P_x = 450\ \mu m$, the two values analyzed in Fig. 2, correspond to $\varepsilon = 37.9\%$ and $\varepsilon = 55.2\%$, respectively). (3) For ε close to 27.6%, the periodicity P_x directs the T_{+1} scattering order to approximately parallel to the air-PDMS surface, and the gap g creates large-angle scattering for the pillar pair. This combined contribution from P_x and g leads to the large efficiency change between 4.3% and 51.0% in Fig. 4(a).

6. SW Generation in two multi-channel SW converters

Based on the results of a single deformable metagrating discussed in Section 5, we demonstrate in this section two representative multi-channel SW converters (Figs. 5 and 6). Both converters contain multiple (three and four in Figs. 5 and 6, respectively) metagrating channels distributed on a PDMS disk with uniform angular intervals. Each channel is a rectangular array of 4 (along the radial direction) by 5 (along the azimuthal direction) unit cells. The values of P_x, g, and P_y follow those in Section 5, which are 290 μm (along the radial direction), 19 μm, and 174 μm (along the azimuthal direction), respectively, without any substrate deformation. The whole disk is uniformly illuminated by left-handed circularly polarized light, and the beam axis passes through the center of the disk.

Without any deformation, the two converters possess rotational symmetry in the *xy* plane, which is 3-fold and 4-fold for the device in Figs. 5 and 6, respectively. As the incident light now also possesses rotational symmetry in the *xy* plane (a feature absent in the *x*-polarized light used in Sections 3-5), the SW conversion efficiency is identical for all the channels in both converters. Applying uniaxial stress on the disk [here along the *x* axis for both devices, as indicated in Figs. 5(c) and 6(c)] breaks this symmetry, and induces directional SW coupling in both converters.

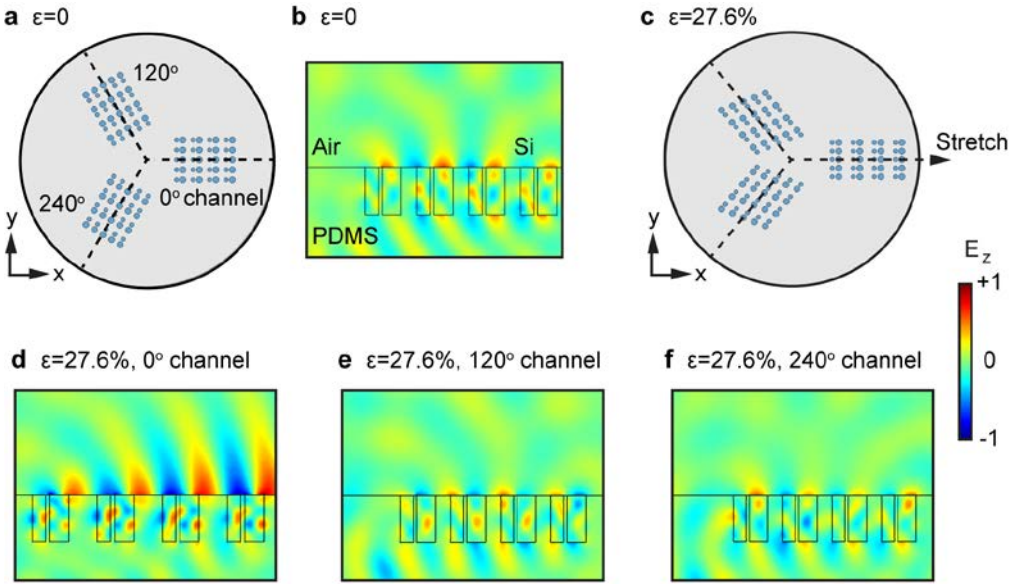

Fig. 5. Directional SW conversion in a disk-shaped, three-channel converter. With strain ε at zero, the inner and outer edges of each metagrating are 290 μm and 1450 μm from the disk center, respectively. The converter is illuminated by left-handed circularly polarized light along the converter axis, and the light beam has a width of 3.7 mm. (a) Schematic of the converter viewed from the top, without any substrate deformation. The dashed lines pass through the center of respective metagratings. (b) E_z field distribution of the 0° channel, taken along the horizontal dashed line in the schematic. The other two channels have the same distribution as here. (c) Schematic of the converter after stretching the substrate along the *x* axis. (d-f) E_z field distributions for the three output channels, taken along the central lines of the metagratings.

The first converter contains three metagrating channels arranged at a uniform angular interval of 120° (Fig. 5). At strain $\varepsilon = 0$, these three channels show an identical near-field distribution due to their planar rotational symmetry, with one representative channels shown in Fig. 5(b). No SW is discernable in these channels, as the geometric dimensions do not favor the SW generation. Figures 5(d)-5(f) show the corresponding field distributions under substrate deformation, with the uniaxial strain along the *x* axis reaching 27.6%. This amount of strain creates the optimal grating configurations for SW conversion in the 0° channel (i.e. $P_x = 370$ μm, $g = 24$ μm, and $P_y = 150$ μm). Strong SW is consequently observed in this channel in Fig. 5(d). By comparison, as the other two channels form a large angle of 120° with the stretch direction, their unit cells are slightly compressed along the radial direction, assuming a uniform compression along the *y* axis. Such grating deformation does not favor SW generation, and SW remains absent in these two channels [Fig. 5(e) and (f)].

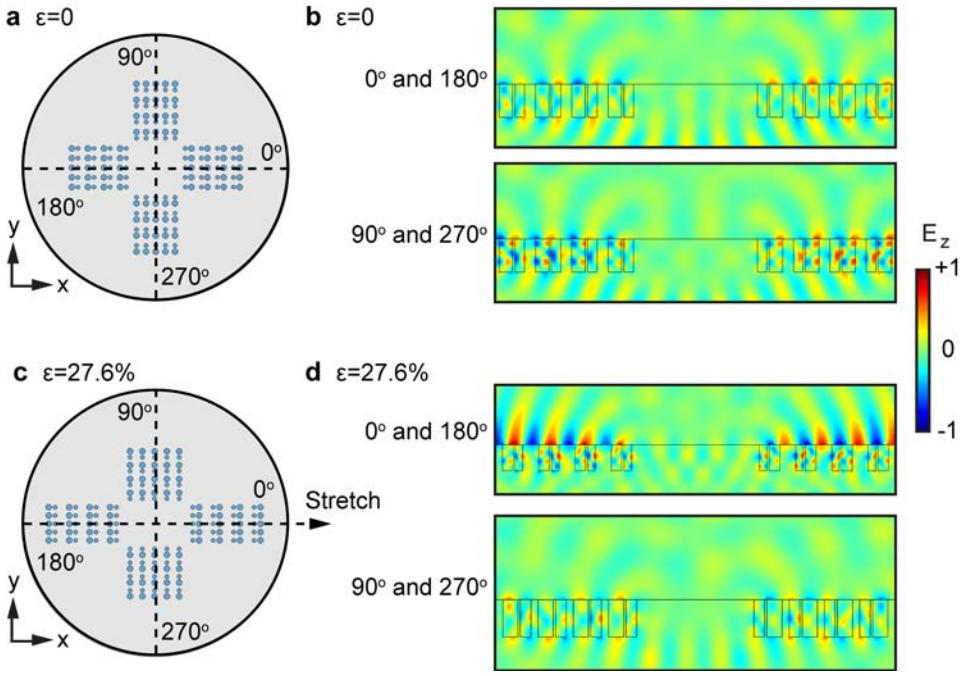

Fig. 6. Directional SW conversion in a disk-shaped, four-channel converter. Without stretching, the inner and outer edges of each metagrating are 435 μm and 1595 μm away from the disk center, respectively. The width of the incident light is now 4.07 mm, to accommodate the change in the spatial span of all the metagratings. (a) Schematic of the converter viewed from the top, without any substrate deformation. (b) E_z field distributions of the channels, taken along the dashed lines in the schematic. (c) Schematic of the converter after stretching the substrate along the *x* axis. (d) Corresponding E_z field distributions, still taken along the channel axes.

The four-channel converter shows similar contrast among different metagrating channels (Fig. 6). In this device, as there are two channels along the stretch direction (i.e. the *x* axis), the deformation converts the incident light into two SWs propagating in the opposite directions (i.e. along the ±*x* directions). By comparison, the two channels along the *y* axis support no SW before and after the deformation.

Table 1. Power and normalized efficiency for each channel in SW conversion, before and after the substrate deformation. The directivity of the SW converters is obtained based on the power contrast among the channels. The incident light has a power density of 1 W/mm^2.

Converter		Power (W)		Norm. efficiency		Directivity
		Before	After	Before	After	
Three-channel	0°	4.5×10^{-3}	1.7×10^{-1}	1.2%	40.4%	38.6
	120°	4.5×10^{-3}	1.6×10^{-3}	1.2%	0.4%	
	240°	4.5×10^{-3}	7.2×10^{-3}	1.2%	1.7%	
Four-channel	0°	4.9×10^{-3}	1.4×10^{-1}	1.3%	33.1%	6.1
	90°	4.9×10^{-3}	2.3×10^{-2}	1.3%	5.5%	
	180°	4.9×10^{-3}	1.4×10^{-1}	1.3%	33.1%	
	270°	4.9×10^{-3}	2.3×10^{-2}	1.3%	5.5%	

To quantify the SW conversion performance of the two converters, Table 1 lists the power and the normalized efficiency for all the output channels. The input power density is set as 1 W/mm^2, and the output power of each channel is calculated by using an integration window placed at the outer edge of respective metagrating. The same as in Section 4, the window is 500 μm in height and its lower boundary is at the air-PDMS interface. Different from the infinitely large array discussed in Section 4, here the size of each metagrating is very limited. For each

metagrating channel, the four unit cells at either side of the channel are viewed as supporting units for the central 12 cells: they help to confine the SW generated in the central 12 cells along the channel axis; meanwhile, their own SW is less confined and may be more difficult to extract for use in future experiments. (It is expected that in future experiments, a SW out-coupler similar to that shown in Fig. 4 can effectively channel the central part of the SW out of the converter). Based on this view, we set the integration window only as wide as the central cells (e.g. it is 3×150 μm for the 0° channel in both converters after substrate deformation). Both the width and the planar orientation of each integration window follow the deformation of the respective channel.

In addition to the absolute output power, the normalized efficiency is further calculated for each channel. It is the ratio of the output power from the 12 central cells and the incident power illuminating these 12 cells (i.e. the effective metagrating area). It takes in to consideration of the surface area change during the substrate deformation. (It is worth noting that, the normalized efficiency here is not with respect to the total input power, making it a parameter different from the efficiency discussed in Section 5.) Congruent with the symmetry-based analysis above, all the output channels have identical output power and efficiency, if the converters have no deformation.

For the three-channel converter, the deformation increases the SW output power in the 0° channel from 4.5×10^{-3} W to 1.7×10^{-1} W (an increase by a factor of 38), and its normalized efficiency from 1.2% to 40.4% (by a factor of 34). The other two channels stay ineffective in SW generation before and after the deformation. These two channels show a small difference in-between after deformation, which is attributed to the handedness of the circularly polarized incident light (here left-handed) and the small but finite crosstalk between adjacent channels. The normalized efficiency of the 0° channel does not reach the peak efficiency shown in Fig. 4(a) due to several changes, including the light polarization, as well as the relative size of the metagrating and the illumination area.

For the four-channel converter, a similar degree of modulation is observed. The 0° and 180° channels have identical output, and the same applies to the 90° and 270° channels. For both the 0° and 180° channels, the output power increases by a factor of 29 (from 4.9×10^{-3} W to 1.4×10^{-1} W) and the normalized efficiency increases by a factor of 26 (from 1.3% to 33.1%). By contrast, the normalized efficiency of the 90° and 270° channels does not surpass 5.5%, a much smaller value as compared to the 33.1% of the 0° and 180° channels. The maximum normalized efficiency (33.1%) is slightly smaller than that of the three-channel converter (40.4%), which is attributed to the finite crosstalk between the channels.

To allow for straightforward evaluation of the degree of directional SW generation in this kind of converters, we utilize a parameter termed as directivity. It is defined as the output power of the most efficient channel(s) divided by the average output power of all the other channels. For both converters, the directivity is 1 without substrate deformation (i.e. all the output channels are equally efficient in SW conversion). With the controlled deformation, the value is $1.7 \times 10^{-1}/((1.6 \times 10^{-3} + 7.2 \times 10^{-3})/2) \approx 38.6$ for the three-channel converter, and $1.4 \times 10^{-1}/2.3 \times 10^{-2} \approx 6.1$ for the four-channel converter. These two values mean that the selected channel(s) in these two channels can be 38.6 and 6.1 times as effective in SW conversion as the average of the other channels.

7. Conclusion

To conclude, we have designed an all-dielectric metagrating that enables high-efficiency, controllable generation of SW from a THz incident wave. The metagrating is an array of Si pillars embedded in a deformable PDMS substrate, and its unit cell contains a pair of closely spaced Si pillars. Its SW conversion efficiency strongly depends on the grating periodicity along the SW propagating direction, as well as the inter-pillar gap size. Applying uniaxial strain along the propagation direction changes both the periodicity and the gap. The conversion efficiency

under the illumination of a linearly polarized light, defined as the power ratio of the SW and the total input, changes between 4.3% and 51.0%.

By using the metagratings as elementary channels, we have also designed two multichannel SW converters that show directional SW generation. Without any substrate deformation, all the channels are ineffective in SW conversion. Stretching the converters along a designated channel creates strong SW in this channel, while the channels misaligned with the stretch direction remains ineffective in SW conversion. This selected channel can reach a normalized SW generation efficiency of 40.4%. As compared to the average of the other channels, it can be up to 38.6 times more effective in SW conversion.

The metagratings and SW converters proposed here could be fabricated using methods similar to those developed for elastic metalenses [35,36]. To redesign the devices for a different wavelength, the initial parametric search discussed in Section 3 can be replaced by simply rescaling all the geometric parameters proportionally to the wavelength. The PW-SW conversion efficiency may be further improved by using optimization schemes such as topology optimization [37], evolutionary optimization [38] and deep learning [39].

The SW propagates on a low-loss interface and most of its energy is concentrated in the air side, making it attractive for many applications in THz communications and sensing. The deformable metagratings and the directional multichannel convertors presented here may be useful for compact and tunable PW-SW couplers, optical modulators and optoelectronic sensors in the THz regime.

Funding

National Natural Science Foundation of China (Grant Nos. 61927804, 61675111 and 61575103); the National Key R&D Program of China (Grant No. 2016YFC0801200); Royal Society (Grant Nos. IEC\R3\183071 and IES\R3\183086).

Data availability

Data underlying the results presented in this paper are not publicly available at this time but may be obtained from the authors upon reasonable request.

Disclosures

The authors declare no conflicts of interest.

See Supplement 1 for supporting content.

References

1. S. Sun, Q. He, S. Xiao, Q. Xu, X. Li, and L. Zhou, "Gradient-index meta-surfaces as a bridge linking propagating waves and surface waves," Nature Materials **11**(5), 426-431 (2012).
2. W. Sun, Q. He, S. Sun, and L. Zhou, "High-efficiency surface plasmon meta-couplers: concept and microwave-regime realizations," Light-Science & Applications **5**(1), e16003 (2016).
3. Z. Wang, S. Li, X. Zhang, X. Feng, Q. Wang, J. Han, Q. He, W. Zhang, S. Sun, and L. Zhou, "Excite Spoof Surface Plasmons with Tailored Wavefronts Using High-Efficiency Terahertz Metasurfaces," Advanced Science **7**(19), 2000982 (2020).
4. A. Pors, M. G. Nielsen, T. Bernardin, J. Weeber, and S. I. Bozhevolnyi, "Efficient unidirectional polarization-controlled excitation of surface plasmon polaritons," Light-Science & Applications **3**(8), e197 (2014).
5. Q. Xu, X. Zhang, M. Wei, G. Ren, Y. Xu, Y. Li, H. Wang, C. Ouyang, J. Han, and W. Zhang, "Efficient Metacoupler for Complex Surface Plasmon Launching," Advanced Optical Materials **6**(5), 1701117 (2018).
6. X. Li, G. Cheng, D. Yan, X. Hou, G. Qiu, J. Li, J. Li, S. Guo, W. Zhou, "One-dimensional terahertz dielectric gradient metasurface for broadband spoof surface plasmon polaritons couplers," Optics Letters **46**(2), 290-293 (2021).
7. H. T. Chen, A. J. Taylor, N. Yu, "A review of metasurfaces: Physics and applications," Reports on Progress in Physics **79**(7), 076401 (2016).

8. S. M. Kamali, E. Arbabi, A. Arbabi, and A. Faraon, “A review of dielectric optical metasurfaces for wavefront control,” Nanophotonics **7**(6), 1041-1068 (2018).
9. W. T. Chen, A. Y. Zhu, F. Capasso, “Flat Optics with Dispersion-Engineered Metasurfaces.” Nature Reviews Materials **5**(8), 604-620 (2020).
10. N. K. Grady, J. E. Heyes, D. R. Chowdhury, Y. Zeng, M. T. Reiten, A. K. Azad, A. J. Taylor, D. A. R. Dalvit, and H. T. Chen, “Terahertz Metamaterials for Linear Polarization Conversion and Anomalous Refraction,” Science **340**(6138), 1304-1307 (2013).
11. X. Ni, N. K. Emani, A. V. Kildishev, A. Boltasseva, and V. M. Shalaev, “Broadband Light Bending with Plasmonic Nanoantennas,” Science **335**(6067), 427 (2012).
12. Y. J. Tsai, S. Larouche, T. Tyler, G. Lipworth, N. M. Jokerst, and D. R. Smith, “Design and fabrication of a metamaterial gradient index diffraction grating at infrared wavelengths,” Optics Express **19**(24), 24411-24423 (2011).
13. M. Khorasaninejad, W. T. Chen, R. C. Devlin, J. Oh, A. Y. Zhu, and F. Capasso, “Metalenses at visible wavelengths: Diffraction-limited focusing and subwavelength resolution imaging,” Science **352**(6290), 1190-1194 (2016).
14. P. R. West, J. L. Stewart, A. V. Kildishev, V. M. Shalaev, V. V. Shkunov, F. Strohkendl, Y. A. Zakharenkov, R. K. Dodds, and R. Byren, “All-dielectric subwavelength metasurface focusing lens,” Optics Express **22**(21), 26212-26221 (2014).
15. S. Yin, F. He, W. Kubo, Q. Wang, J. Frame, N. G. Green and X. Fang, “Coherently tunable metalens tweezers for optofluidic particle routing,” Optics Express **28**(26), 38949-38959 (2020).
16. M. Khorasaninejad, A. Ambrosio, P. Kanhaiya, and F. Capasso, “Broadband and chiral binary dielectric meta-holograms,” Science Advances **2**(5), e1501258 (2016).
17. B. Desiatov, N. Mazurski, Y. Fainman, and U. Levy, “Polarization selective beam shaping using nanoscale dielectric metasurfaces.” Optics Express **23**(17), 22611-22618 (2015).
18. J. P. Balthasar Mueller, K. Leosson, and F. Capasso, “Ultracompact metasurface in-line polarimeter,” Optica **3**(1), 42-47 (2016).
19. N. Yu, P. Genevet, M. A. Kats, F. Aieta, J. P. Tetienne, F. Capasso, and Z. Gaburro, “Light Propagation with Phase Discontinuities Reflection and Refraction,” Science **334**(6054), 333-337 (2011).
20. S. Sun, K. Y. Yang, C. M. Wang, T. K. Juan, W. T. Chen, C.Y. Liao, Q. He, S. Xiao, W. T. Kung, G. Y. Guo, L. Zhou, and D. P. Tsai, “High-efficiency broadband anomalous reflection by gradient meta-surfaces,” Nano Letters **12**(12), 6223-6229 (2012).
21. S. Q. Li, X. Xu, R. M. Veetil, V. Valuckas, R. Paniagua-Dominguez, and A. I. Kuznetsov, "Phase-only transmissive spatial light modulator based on tunable dielectric metasurface," Science **364**(6445), 1087-1090 (2019).
22. W. Yang, S. Xiao, Q. Song, Y. Liu, Y. Wu, S. Wang, J. Yu, J. Han, and D. P. Tsai, “All-dielectric metasurface for high-performance structural color,” Nature Communications **11**(1), 1864 (2020).
23. Y. F. Yu, A. Y. Zhu, R. Paniagua-Domínguez, Y. H. Fu, B. Luk’yanchuk, and A. I. Kuznetsov, “High-transmission dielectric metasurface with 2π phase control at visible wavelengths,” Laser & Photonics Reviews **9**(4), 412-418 (2015).
24. D. Sell, J. Yang, S. Doshay, R. Yang, and J. A. Fan, “Large-Angle, Multifunctional Metagratings Based on Freeform Multimode Geometries,” Nano Letters **17**(6), 3752-3757 (2017).
25. F. He, K. F. Macdonald, and X. Fang, “Continuous beam steering by coherent light-by-light control of dielectric metasurface phase gradient,” Optics Express **28** (20), 30107-30116 (2020).
26. J. Dai, J. Zhang, W. Zhang, and D. Grischkowsky, “Terahertz time-domain spectroscopy characterization of the far-infrared absorption and index of refraction of high-resistivity, float-zone silicon,” Journal of The Optical Society of America B-Optical Physics **21**(7), 1379-1386 (2004).
27. I. E. Khodasevych, C. M. Shah, S. Sriram, M. Bhaskaran, W. Withayachumnankul, B. S. Y. Ung, H. Lin, W. S. T. Rowe, D. Abbott, and A. Mitchell, “Elastomeric silicone substrates for terahertz fishnet metamaterials,” Applied Physics Letters **100**(6), 61101 (2012).
28. R. Paniagua-Domínguez, Y. F. Yu, E. Khaidarov, S. Choi, V. Leong, R. M. Bakker, X. Liang, Y. H. Fu, V. Valuckas, L. A. Krivitsky, and A. I. Kuznetsov, “A Metalens with a Near-Unity Numerical Aperture,” Nano Letters **18**(3), 2124-2132 (2018).
29. A. Patri, S. Kéna-Cohen, and C. Caloz, “Large-Angle, Broadband, and Multifunctional Directive Waveguide Scatterer Gratings,” ACS Photonics **6**(12), 3298-3305 (2019).
30. J. Li, T. Wu, W. Xu, Y. Liu, C. Liu, Y. Wang, Z. Yu, D. Zhu, L. Yu, and H. Ye, “Mechanisms of 2π phase control in dielectric metasurface and transmission enhancement effect,” Optics Express **27**(16), 23186-23196 (2019).
31. B. Wu, A. Kumar, and S. Pamarthy, “High aspect ratio silicon etch: A review,” Journal of Applied Physics **108**(5), 51101 (2010).
32. A. Müller, M. C. Wapler, and U. Wallrabe, “A quick and accurate method to determine the Poisson’s ratio and the coefficient of thermal expansion of PDMS,” Soft Matter **15**(4), 779-784 (2019).
33. S. Liu, H. C. Zhang, L. Zhang, Q. L. Yang, Q. Xu, J. Gu, Y. Yang, X. Y. Zhou, J. Han, Q. Cheng, W. Zhang, T. J. Cui, “Full-State Controls of Terahertz Waves Using Tensor Coding Metasurfaces,” ACS Applied Materials & Interfaces **9**(25), 21503-21514 (2017).
34. I. Johnston, D. McCluskey, C. Tan, and M. C. Tracey, “Mechanical characterization of bulk Sylgard 184 for microfluidics and microengineering,” Journal of Micromechanics and Microengineering **24**(3), 35017 (2014).

35. H. S. Ee and R. Agarwal, "Tunable Metasurface and Flat Optical Zoom Lens on a Stretchable Substrate," Nano Lett **16**, 2818-2823 (2016).
36. S. M. Kamali, E. Arbabi, A. Arbabi, Y. Horie, and A. Faraon, "Highly tunable elastic dielectric metasurface lenses," Laser Photonics Rev **10**, 1002-1008 (2016).
37. J. S. Jensen and O. Sigmund, "Topology optimization for nano-photonics," Laser Photonics Rev **5**, 308-321 (2011).
38. M. D. Huntington, L. J. Lauhon, and T. W. Odom, "Subwavelength Lattice Optics by Evolutionary Design," Nano Lett. **14**, 7195-7200 (2014).
39. S. Inampudi and H. Mosallaei, "Neural network based design of metagratings," Appl. Phys. Lett. **112**, 241102 (2018).